Energy response characterization of InGaP X-ray detectors

Article (Accepted Version)

Energy response characterization of InGaP X-ray detectors

G. Lioliou[1a)], A.B. Krysa[2], and A. M. Barnett[1]

[1]Space Research Group, Sch. of Engineering and Informatics, University of Sussex, Falmer, Brighton, BN1 9QT, UK

[2]EPSRC National Epitaxy Facility, University of Sheffield, Mappin Street, Sheffield, S1 3JD, UK

Two custom-made $In_{0.5}Ga_{0.5}P$ p^+-i-n^+ circular mesa spectroscopic X-ray photodiodes with different diameters (200 μm and 400 μm) and a 5 μm i layer have been characterized for their response to X-ray photons within the energy range 4.95 keV to 21.17 keV. The photodiodes, operating uncooled at 30 °C, were coupled, in turn, to the same custom-made charge-sensitive preamplifier. X-ray fluorescence spectra of high-purity calibration foils excited by a Mo target X-ray tube were accumulated. The energy resolution (*Full Width at Half Maximum*) increased from 0.79 keV ± 0.02 keV at 4.95 keV to 0.83 keV ± 0.02 keV at 21.17 keV, and from 1.12 keV ± 0.02 keV at 4.95 keV to 1.15 keV ± 0.02 keV at 21.17 keV, when using the 200 μm and 400 μm diameter devices, respectively. Energy resolution broadening with increasing energy was attributed to increasing Fano noise (negligible incomplete charge collection noise was suggested); for the first time the Fano factor for $In_{0.5}Ga_{0.5}P$ was experimentally determined to be 0.13, suggesting a Fano limited energy resolution of 145 eV at 5.9 keV. The charge output of each system had a linear relationship with photon energy, across the investigated energy range. The count rate of both spectroscopic systems increased linearly with varying X-ray tube current up to ~10^5 photons s^{-1} cm^{-2} incident photon fluences. The development of $In_{0.5}Ga_{0.5}P$ based spectrometers is particularly important for hard X-/γ-ray astronomy, due to the material's large linear X-ray and γ-ray absorption coefficients and ability to operate uncooled at high temperatures.

I. INTRODUCTION

$In_{0.5}Ga_{0.5}P$ is a promising new material for future high temperature tolerant X-ray photodiodes. One of $In_{0.5}Ga_{0.5}P$'s favourable attributes is its relatively wide bandgap (~1.9 eV at room temperature [1]). The number of thermally generated carriers in a wide bandgap material can be lower than in materials with narrower bandgaps at a given temperature [2]. Since the leakage current of photodiode detectors is fundamentally tied to the number of thermally generated carriers within the detector, wide bandgap X-ray detectors can be used at high temperatures (≥ 20 °C) without the need for cooling systems. Much ongoing research world-wide concerns the development of wide bandgap materials for high temperature tolerant X-ray detectors, including GaAs [3-5], 4H-SiC [6-8], AlGaAs [9] [10], AlInP [11] [12], HgI_2 [13], TlBr [14], and CdTe and CdZnTe [15-17]. Applications which would benefit from the development of wide bandgap X-ray detectors include those with limitations on the mass, volume, power and/or cost of the instrumentation since elimination of the cooling systems and shielding which

a) Corresponding author. Tel.: +44 (0) 1273 872568. E-mail address: G.Lioliou@sussex.ac.uk

are often required for narrower bandgap detectors would produce real advantages. Applications in space science and astronomy are particular motivations.

$In_{0.5}Ga_{0.5}P$ is almost completely lattice matched to GaAs (< ± 0.1% lattice mismatch) [18]. Thus, high quality $In_{0.5}Ga_{0.5}P$ structures can be epitaxially grown on GaAs substrates. Also, $In_{0.5}Ga_{0.5}P$ benefits from a high density, which is almost twice that of Si (4.5 g/cm^3 for $In_{0.5}Ga_{0.5}P$ cf. 2.33 g/cm^3 for Si) [19]). The high density of $In_{0.5}Ga_{0.5}P$ along with the presence of In (atomic number of 49), results in better stopping power and higher quantum efficiency per unit thickness compared to Si, SiC, GaAs, and $Al_{0.52}In_{0.48}P$ [20]. This is particularly significant at higher photon energies. For instance, the linear absorption coefficient at 60 keV for $In_{0.5}Ga_{0.5}P$ (15.99 cm^{-1}) is greater than those for Si (0.75 cm^{-1}), Ge (10.77 cm^{-1}), and GaAs (10.84 cm^{-1}), and almost comparable to $Cd_{1-x}Zn_xTe$ (ranging from 30.36 cm^{-1} to 37.81 cm^{-1}, depending on the fraction x) [21]. Hence, there is a potentially significant utility for $In_{0.5}Ga_{0.5}P$ detectors within future planetary and astrophysics missions, which require detection of hard X-rays and γ-rays. CdZnTe detectors have been used for such applications [22] [23], but can suffer performance degradation. For example, Te inclusions and polarization effects within $Cd_{1-x}Zn_xTe$ detectors [16] can cause degradation in spectral response (e.g. a relatively modest 1.6 keV *Full Width at Half Maximum* (*FWHM*) at 5.9 keV was achieved at 23 °C [24] and 1.8 keV *FWHM* (without tail) at 59.54 keV was achieved at 21 °C [17], despite significant worldwide efforts to develop improved CdZnTe detectors). The best energy resolution ever recorded using a CdTe detector at room temperature, was 843 eV *FWHM* at 59.54 keV [25]; the CdTe pixel detector was coupled to an ultra low noise CMOS charge sensitive preamplifier (1.2 e$^-$ rms equivalent noise charge with no detector connected).

Despite the desirable attributes of $In_{0.5}Ga_{0.5}P$, very little work has been carried out on the material in regards to the development of X-ray and γ-ray detectors. The first $In_{0.5}Ga_{0.5}P$ X-ray detectors were reported by Butera et al. [26]; an *FWHM* at 5.9 keV of 900 eV was achieved with the detectors and preamplifier operating at room temperature. $In_{0.5}Ga_{0.5}P$ X-ray detectors have also been investigated for high temperature X-ray spectroscopy, reporting an energy resolution of 1.27 keV *FWHM* at 5.9 keV, at 100 °C, and 770 eV *FWHM* at 5.9 keV, at 20 °C [27]. The $In_{0.5}Ga_{0.5}P$ electron hole pair creation energy was experimentally measured between 100 °C and 20 °C by Butera et al. [27], and found to be 4.94 eV ± 0.06 eV at 20 °C. Work has been conducted on $In_{0.5}Ga_{0.5}P$'s binary relations, GaP [28] and InP [29] [20], but both were not spectroscopic at room temperature. A GaP Schottky diode showed a response to hard X-rays (11 keV to 100 keV) at room temperature, but the individual energies were not spectrally resolved [28]. InP detectors showed a spectroscopic response when cooled to low temperatures: a *FWHM* at 5.9 keV of 2.5 keV was measured at -60 °C [29], and a *FWHM* at 59.5 keV of 7 keV

was measured at -57 °C [20]. It should be noted here that the InP detectors reported in Refs. [29] [20] were not epitaxially grown but they were based on bulk semi-insulating InP. The potential use of InP detectors for solar neutrino detection has also been discussed; for example an In based detector may allow the detection of the characteristic signature of the inverse β decay of ^{115}In [30-32].

This paper significantly extends the previous work on $In_{0.5}Ga_{0.5}P$ for X-ray detection. Two $In_{0.5}Ga_{0.5}P$ p^+-i-n^+ circular mesa photodiodes (one with a diameter of 200 μm; one with a diameter of 400 μm) made from the same material as reported in Ref. [26] [27] were characterized for their response to illumination with X-rays within the energy range 4.95 keV to 21.17 keV. A Mo target X-ray tube and 9 high-purity metal fluorescence foils were used (in turn) to generate characteristic X-ray fluorescence lines which illuminated the detectors. The photodiodes were connected, in turn, to the same custom-made low-noise single channel charge-sensitive preamplifier. The X-ray fluorescence spectra accumulated with each X-ray spectrometer enabled the determination of the Fano factor of $In_{0.5}Ga_{0.5}P$. The response of each X-ray spectrometer was also investigated at five different fluences of X-ray photons at energies of 8.63 keV and 16.6 keV. The temperature of the detectors and preamplifier during the measurements was 30 °C ± 3 °C.

II. DEVICE STRUCTURE

An $In_{0.5}Ga_{0.5}P$ p^+-i-n^+ epilayer was grown on a (100) heavily doped n^+ GaAs substrate by metalorganic vapour phase epitaxy (MOVPE) using trimethylgallium, trimethylindium, arsine, and phosphine as precursors, and hydrogen as a carrier gas. The spontaneous long-range ordering in the group III sublattice and related effects on the bandgap [33] [34] were avoided by a miscut angle of 10 ° towards <111>A at the epitaxial surface of the substrate. The p^+ layer, the unintentionally doped i layer, and the n^+ layer had thicknesses of 0.2 μm, 5 μm, and 0.1 μm, respectively. The doping concentration of both the p^+ and n^+ layers was $\approx 2 \times 10^{18}$ cm^{-3}. A p^+ GaAs layer with a thickness of 0.01 μm (1×10^{19} cm^{-3} doping concentration) was grown on top of the $In_{0.5}Ga_{0.5}P$ p^+-i-n^+ epilayer, to help enable formation of a good top Ohmic contact. A quasi-annular top Ohmic contact consisting of 20 nm of Ti and 200 nm of Au was deposited on the top face of each of the detectors. A planar rear Ohmic contact consisting of 20 nm of InGe and 200 nm of Au was deposited on the rear of the substrate. The fabrication of the 200 μm diameter and 400 μm diameter $In_{0.5}Ga_{0.5}P$ mesa devices used in this study was achieved with chemical wet etching techniques. A 1:1:1 $K_2Cr_2O_7$:HBr:CH_3COOH solution followed by a 10 s finishing etch in 1:8:80 H_2SO_4:H_2O_2:H_2O solution was used. The top Ohmic contact covered 45 % of the surface of the 200 μm diameter devices and 33 % of the 400 μm diameter devices. The $In_{0.5}Ga_{0.5}P$ photodiodes were not passivated. Both

detectors were on the same die. The die was packaged in a TO-5 can and gold-ball wirebonded. The wafer's layer structure is summarised in **TABLE I**.

TABLE I. Layers structure of the $In_{0.5}Ga_{0.5}P$ p^+-i-n^+ wafer.

Material	Type	Thickness (nm)	Doping density (cm^{-3})
GaAs	p^+	10	1×10^{19}
$In_{0.5}Ga_{0.5}P$	p^+	200	2×10^{18}
$In_{0.5}Ga_{0.5}P$	i	5000	undoped
$In_{0.5}Ga_{0.5}P$	n^+	100	2×10^{18}
GaAs	n^+ (substrate)	-	-

III. ELECTRICAL CHARACTERIZATION

The dark current and capacitance as functions of applied reverse bias of the $In_{0.5}Ga_{0.5}P$ photodiodes were measured prior to illuminating the devices with X-rays. To do this, the diodes were installed inside a TAS Micro MT climatic cabinet for temperature control. The properties of the devices were measured at 33 °C, 30 °C, and 27 °C, since the X-ray measurements were to be conducted at a temperature of 30 °C ± 3 °C. To ensure thermal equilibrium, the diodes were left to stabilize at each temperature for 30 minutes before the measurements were started at each temperature. Dry N_2 was continually flowed into the climatic cabinet throughout the measurements to maintain a dry environment (< 5 % relative humidity). Dark currents were measured using a Keysight B2981A Femto/Picoammeter as functions of applied reverse bias, V_{AR}, from 0 V to -30 V. The reverse bias was applied using a Keithley 2636B SourceMeter. The uncertainty associated with each current reading was 1% of the measurement plus 3 fA [35]. The uncertainty associated with the applied reverse bias was 0.02% of the applied bias plus 50 mV [36]. The leakage current associated with the TO-5 package was also measured as a function of bias and temperature, and subtracted from the leakage current of the packaged photodiodes to yield the leakage current of each diode alone. The leakage currents of the packaged $In_{0.5}Ga_{0.5}P$ p^+-i-n^+ diodes, as well as the leakage currents of the diodes themselves (with the leakage current of the package subtracted) at 30 °C can be seen in **Fig. 1**. The equivalent noise charge of the white parallel noise, ENC_{WP}, at a shaping time of 6 μs, as calculated from the leakage current of the detector (see Section **IV. ENERGY LINEARITY MEASUREMENTS**) can also be seen in **Fig. 1**.

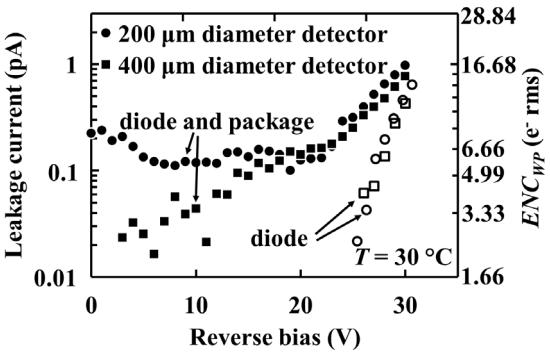

FIG. 1. Leakage current and calculated ENC_{WP} at 6 µs shaping time as a function of applied reverse bias of the 200 µm (circles) and the 400 µm (squares) diameter $In_{0.5}Ga_{0.5}P$ p^+-i-n^+ mesa photodiode, with (filled symbols) and without (empty symbols) the leakage current of the package, at 30 °C.

The leakage current of the packaged $In_{0.5}Ga_{0.5}P$ 200 µm diameter device at -30 V reverse bias, at 33 °C, 30 °C, and 27 °C, was measured to be 1.0 pA ± 0.5 pA (rms deviance). Similarly, the leakage current of the packaged $In_{0.5}Ga_{0.5}P$ 400 µm diameter device at -30 V reverse bias was measured to be 0.8 pA ± 0.4 pA (rms deviance), at the same temperatures. The leakage current of both packaged diodes remained ≤ 0.2 pA (≤ 8 e^- rms ENC_{WP} at 6 µs) at -5 V reverse bias, the reverse bias applied during X-ray measurements. The leakage current of the $In_{0.5}Ga_{0.5}P$ p^+-i-n^+ mesa photodiodes themselves (i.e. with the leakage current of the package subtracted) at the highest investigated reverse bias (-30 V), at 33 °C, was 1.249 pA ± 0.004 pA (corresponding to a leakage current density of 3.97 nA/cm^2 ± 0.01 nA/cm^2) and 0.966 pA ± 0.004 pA (corresponding to a leakage current density of 0.769 nA/cm^2 ± 0.003 nA/cm^2) for the 200 µm and 400 µm diameter device, respectively.

Detector capacitances were measured in dark conditions using an HP 4275A Multi-Frequency LCR meter with 50 mV rms magnitude and 1 MHz frequency test signal. The reverse bias, V_{AR}, from 0 V to -30 V, was applied during the capacitance measurements using a Keithley 6487 Picoammeter/Voltage Source. The uncertainty associated with the capacitance reading was (0.1% + 3 fF) × 1.2 [37]. The uncertainty associated with the applied reverse bias was 0.1% of the applied bias plus 4 mV [38]. The total uncertainty of the capacitance measurements of the packaged devices was estimated to be ± 0.02 pF. The $In_{0.5}Ga_{0.5}P$ p^+-i-n^+ packaged diode capacitance as a function of applied reverse bias at 30 °C can be seen in **Fig. 2**. The equivalent noise charge of the white series noise, ENC_{WS}, as calculated to arise from the capacitance of the $In_{0.5}Ga_{0.5}P$ p^+-i-n^+ photodiode detector at a shaping time of 6 µs (see Section **IV. ENERGY LINEARITY MEASUREMENTS**), can also be seen in **Fig. 2**.

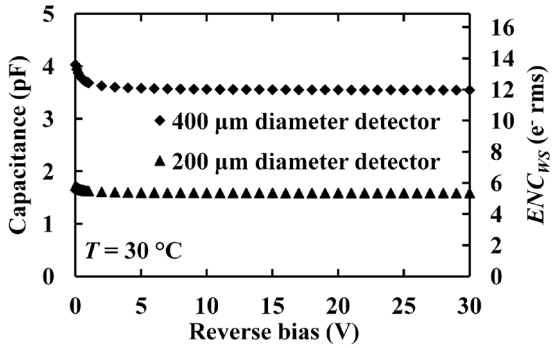

FIG. 2. Capacitance and calculated ENC_{WS} at 6 µs shaping time as a function of applied reverse bias of the packaged 200 µm (triangles) and the 400 µm (diamonds) diameter $In_{0.5}Ga_{0.5}P$ p^+-i-n^+ mesa photodiodes, at 30 °C.

The capacitance of the packaged 200 µm diameter $In_{0.5}Ga_{0.5}P$ p^+-i-n^+ photodiode was found to decrease from 1.72 pF ± 0.02 pF at no applied bias to 1.59 pF ± 0.02 pF at -30 V applied reverse bias. Similarly, the capacitance of the 400 µm diameter $In_{0.5}Ga_{0.5}P$ p^+-i-n^+ photodiode was found to decrease from 4.03 pF ± 0.02 pF at no applied bias to 3.55 pF ± 0.02 pF at -30 V applied reverse bias. No variation of capacitance with temperature was observed for either diode within the investigated temperature range, 33 °C to 27 °C. Assuming a packaging capacitance of 0.932 pF ± 0.001 pF, which is consistent with previous measurements of the TO-5 cans packaging capacitance, the capacitance density of both photodiodes was found to be 2.08×10^3 pF cm^{-2} at -30 V applied reverse bias, at 30 °C. Subtracting the packaging capacitance from each packaged detector capacitance, the intrinsic capacitance was found to be 0.66 pF and 2.62 pF, for the 200 µm and the 400 µm diameter $In_{0.5}Ga_{0.5}P$ p^+-i-n^+ photodiode, at -30 V applied reverse bias and a temperature of 30 °C; the ratio of the photodiodes' capacitances (= 4) was consistent with the ratio of the photodiodes' areas. Assuming a parallel plate capacitance, the depletion layer width of each photodiode was calculated as a function of applied reverse bias [39] (see **Fig. 3**). At low applied reverse biases, the depletion layer width of both devices increased as the applied reverse biased increased. Both the 200 µm and the 400 µm diameter $In_{0.5}Ga_{0.5}P$ p^+-i-n^+ mesa photodiodes were found to be fully depleted at -1 V. The depletion layer width at full depletion was calculated from these measurements to be 5.0 µm ± 0.4 µm and 5.0 µm ± 0.4 µm for the 200 µm and the 400 µm diameter device, respectively. The calculated depletion layer width was consistent with that indicated by measurements during the epitaxial growth. The uncertainty in the depletion layer width was determined predominantly by the Debye length (calculated for $In_{0.5}Ga_{0.5}P$ with a doping concentration of 10^{14} cm^{-3} to be 0.4 µm at a temperature of 30 °C [39]). In contrast, the measurement uncertainties in the capacitance measurements, were calculated to be less than ± 0.16 µm and less than ± 0.04 µm for the 200 µm and the 400 µm diameter devices, respectively.

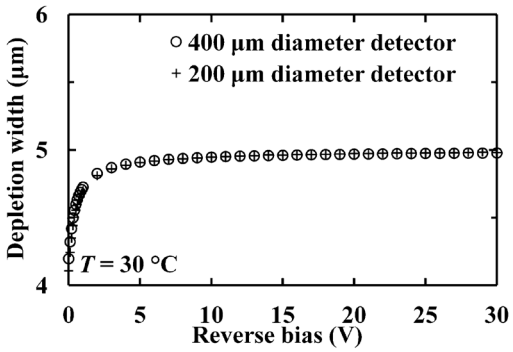

FIG. 3. Calculated depletion layer width as a function of applied reverse bias of the 200 μm (triangles) and the 400 μm (diamonds) diameter $In_{0.5}Ga_{0.5}P$ p^+-i-n^+ mesa photodiodes, measured at 30 °C.

IV. ENERGY LINEARITY MEASUREMENTS

The two $In_{0.5}Ga_{0.5}P$ p^+-i-n^+ mesa photodiode detectors (one with a 200 μm diameter, one with a 400 μm diameter), were each connected, in turn, to the input of the same custom-made single channel charge-sensitive preamplifier. The preamplifier was of feedback resistorless design, similar to Ref. [40]. It had a Vishay Siliconix 2N4416A JFET for the input transistor [41]. The detector and preamplifier were installed in a custom Al enclosure with a 4 μm thick Al window. The Al enclosure was installed within a LD Didactic GmbH X-ray apparatus (part number 554 801) with a Mo target X-ray tube [42]. A custom-made Al collimator, lined with PTFE (to absorb all fluorescence from the Al of the collimator), was used to collimate the X-rays from the Mo target X-ray tube. The Al enclosure was attached to the goniometer of the apparatus for precise positioning. The output of the preamplifier was shaped by an ORTEC 572A shaping amplifier. The output of the shaping amplifier was connected to an ORTEC 927 ASPEC multi-channel analyser (MCA) with 16k channels for digitation. The two X-ray spectrometers had identical electronics, only the detector was different; one spectrometer employed the 200 μm diameter detector and the other spectrometer employed the 400 μm diameter detector.

The energy-charge response linearity of each spectrometer was measured using 9 high purity metal X-ray fluorescence calibration samples of known composition. The samples, along with the accepted energies of the X-ray emission lines, used in the measurements are shown in order of ascending energy in **TABLE II**.

TABLE II. X-ray fluorescence calibration samples used to characterize the energy-charge response linearity of the $In_{0.5}Ga_{0.5}P$ based spectrometers, along with their corresponding X-ray emission line energies.

X-ray fluorescence sample (Primary line used)	Line Energy (keV)
V (Kα)	4.95
Cr (Kα)	5.41
Mn (Kα)	5.89
Cu (Kα)	8.04
Zn (Kα)	8.63
Au (Lα)	9.71
Ge (Kα)	9.88
Au (Lβ)	11.44
Nb (Kα)	16.61
Pd (Kα)	21.17

The X-ray fluorescence calibration samples were positioned on the sample stand of the X-ray apparatus at 45 ° to the collimator. The detector-preamplifier system was positioned at 135 ° to the collimator. This arrangement ensured the maximum detection of X-ray fluorescence from the samples, and minimum detection of X-rays directly from the tube. The X-ray tube voltage and current were set to 35 kV and 1 mA, respectively. X-ray spectra of each foil were accumulated with both spectrometers. The live times were 4 hours and 1 hour, for the spectrometer with the 200 μm and the 400 μm diameter detector respectively, thus in proportion to the detectors' areas. In each case, the detector was reverse biased at -5 V and the shaping time of the shaping amplifier was set to 6 μs.

Gaussians were fitted to the peaks of the spectra accumulated with the foils. The position of the centroid of each fitted fluorescence peak on the MCA scale along with that peak's accepted energy were used to deduce the energy calibrations of both systems. **Figure 4** shows the positions of the peaks' centroids on the MCA scale as a function of photon energy. The lines of best fit were calculated using linear least squares fitting. The error bars, associated with the fitting for each data point, computed to be ± 3 channels and ± 2 channels for the spectrometer employing the 200 μm and 400 μm diameter detector, respectively, were obtained from

$$S = \sqrt{\frac{\Sigma(C_N' - C_N)^2}{n-2}}, \quad (1)$$

where C_N' was the experimentally determined channel number (position of the centroid) of each photopeak, C_N was the channel number as calculated using the linear least squares fitting (see **Fig. 4**), and n was the number of

data points (number of X-ray lines used) for the linear least squares fitting (see **TABLE II**) [43]. The numerator within the square root was the sum of squared residuals, and the denominator was the number of degrees of freedom associated with the sum of squared residuals. Since the error bars were comparable to the inherent analytical uncertainties from experimentally determining the position of the centroid of each peak in the spectra (typically ± 3 channels), it can be said that the voltage outputs of both systems had linear relationships with photon energy. The width of each channel was computed to be 7 eV and 9 eV for the spectrometer employing the 200 μm and 400 μm diameter detector, respectively. The residuals of the fit in percentage terms were also evaluated; they were found to be less than ± 0.3 % and less than ± 0.4 % for the 200 μm and the 400 μm diameter device systems, respectively.

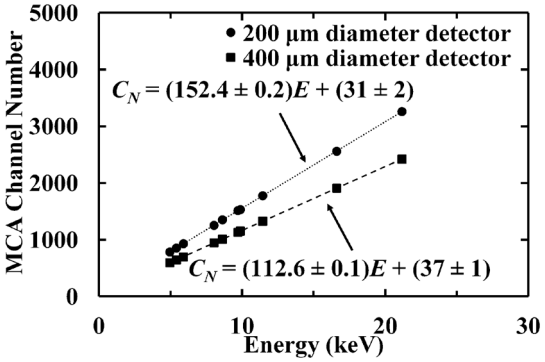

FIG. 4. Position of photopeak centroid, C_N, as a function of energy, E [keV], for the spectrometer employing the $In_{0.5}Ga_{0.5}P$ 200 μm (circles) and 400 μm (squares) diameter detector. The lines of best fit, calculated using linear least squares fitting, can also be seen. The linearity error (evaluated by residuals of the fit) was found to be less than ± 0.3 % and less than ± 0.4 % for the 200 μm and the 400 μm diameter device systems, respectively.

An example X-ray fluorescence spectrum of the Mn foil obtained using the spectrometer with the 200 μm diameter detector, can be seen in **Fig. 5**. The detected peak is the combination of the Mn Kα and Mn Kβ lines, at 5.9 keV and 6.49 keV respectively [44]; the energy resolution was not sufficient to resolve the individual lines. The dashed lines shown in **Fig. 5** represent the Gaussians fitted to the peak taking into account the relative emission ratio [44] and the relative efficiency of the detector at 5.9 keV (Mn Kα) and 6.49 keV (Mn Kβ). The energy calibration of the MCA's charge scale of the spectrum was achieved using the relationship presented in **Fig. 4**. The counts of the zero energy noise peak of the spectrometer were limited by setting the MCA low energy cut-off at 1.7 keV; a small portion of the right hand side of the tail can still be seen in **Fig. 5**. Spectra of this nature were obtained for all of the calibration foils.

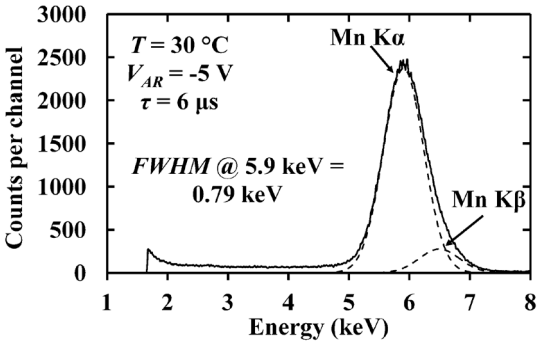

FIG. 5. Mn spectrum accumulated with the spectrometer employing the $In_{0.5}Ga_{0.5}P$ 200 µm diameter detector at -5 V.

The energy resolution of each photopeak in the spectra, accumulated using both spectrometers, was measured, and can be seen in **Fig. 6**. It was found to increase from 0.79 keV ± 0.02 keV at 4.95 keV to 0.83 keV ± 0.02 keV at 21.17 keV, and from 1.12 keV ± 0.02 keV at 4.95 keV to 1.15 keV ± 0.02 keV at 21.17 keV, for the spectrometer employing the 200 µm and the 400 µm diameter detector, respectively. The energy resolution of an X-ray spectrometer consisting of a non-avalanche photodiode detector coupled to a charge sensitive preamplifier is degraded due to Fano noise, electronic noise, and incomplete charge collection noise [45]. The Fano noise, ΔE_F, is energy dependent; it increases with increasing photon energy, E, as per

$$\Delta E_F[\text{eV}] = (8 \ln 2)^{0.5} \omega \sqrt{\frac{FE}{\omega}}, \tag{2}$$

where ω is the electron-hole pair creation energy and F is the Fano factor [46]. The incomplete charge collection noise is also photon energy dependent, whereas the electronic noise is photon energy invariant. The incomplete charge collection noise was found to be negligible at -5 V reverse bias [26], thus the quadratic sum of the Fano noise and the electronic noise, ΔE_E,

$$\Delta E\ [\text{eV}] = \sqrt{(8 \ln 2\ \omega F E) + {\Delta E_E}^2}, \tag{3}$$

defined the *FWHM*. The Fano factor and the electronic noise were determined by fitting **Eq. 3** to the measured *FWHM* as a function of energy (**Fig. 6**), assuming an electron hole pair creation energy of 4.95 eV ± 0.07 eV at 300 K [27]. The minimization of the sum of the squares of the residuals between the fitting and the measured *FWHM* for both spectrometers suggested a Fano factor of 0.13. This value is comparable to Fano factor values previously reported for other semiconductors such as 4H-SiC (= 0.10) [6], Si (= 0.12) [47], Ge (= 0.11) [47], GaAs (= 0.12 - 0.14) [48] [49], and CdTe (= 0.15) [50]. The Fano noise was calculated to increase from 133 eV at 4.95 keV to 275 eV at 21.17 keV, and to be 145 eV at 5.9 keV. The electronic noise was calculated to be 0.77 keV ± 0.02 keV and 1.13 keV ± 0.02 keV within the investigated energy range, for the spectrometer employing

the $In_{0.5}Ga_{0.5}P$ 200 μm and the 400 μm diameter detector, respectively. Its rms deviance, attributed to the error in fitting the photopeaks, was estimated to be ± 0.02 keV. The quadratic sum of the derived electronic noise and the calculated Fano noise, comprising the predicted *FWHM*, can be seen in **Fig. 6**. Since these values were in good agreement with the measured *FWHM*, the increase of the *FWHM* with increased energy was solely attributed to the increase of the Fano noise, and thus, the absence of significant incomplete charge collection noise was confirmed.

The white parallel noise (arising from the leakage current), ENC_{WP}, and white series noise (arising from the capacitance), ENC_{WS}, contributions of the $In_{0.5}Ga_{0.5}P$ detectors were calculated according to Lioliou & Barnett [45], at 6 μs shaping time, and can be seen in **Fig. 1** and **Fig. 2**, respectively. The ENC_{WP} was calculated to be ≤ 8 e^- rms for both $In_{0.5}Ga_{0.5}P$ detectors. However, the ENC_{WS} was calculated to vary among the two different diameter devices, due to their different capacitances; 5 e^- rms and 12 e^- rms at 6 μs and at -5 V reverse bias were calculated for the 200 μm and the 400 μm diameter device, respectively. The difference in electronic noise between the two spectrometers was attributed to the higher capacitance of the 400 μm diameter device compared to the capacitance of the 200 μm diameter device, resulting in higher white series noise (ENC_{WS}) and dielectric noise (proportional to the capacitance of the lossy dielectrics, including the semiconductor photodiodes themselves [45]) in the spectrometer employing the 400 μm diameter devices compared to that with the 200 μm diameter device.

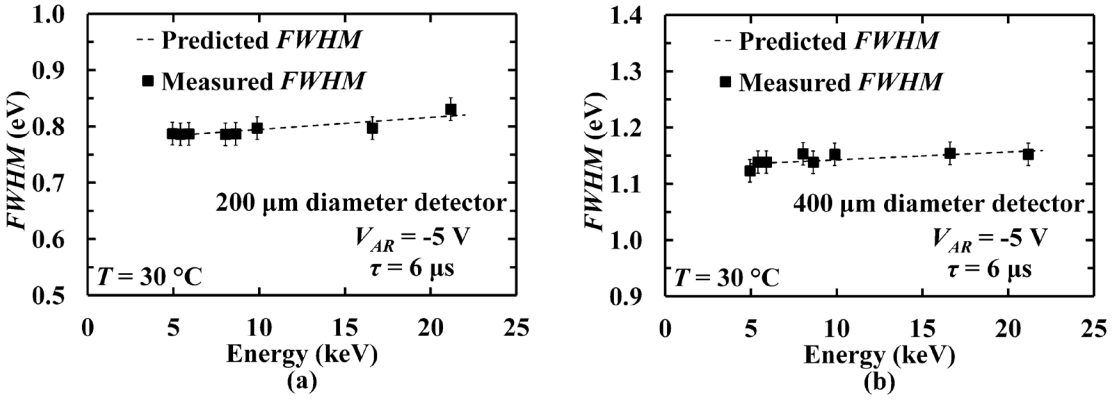

FIG. 6. Measured *FWHM* (filled squares) across the investigated energy range with the spectrometer employing the $In_{0.5}Ga_{0.5}P$ (a) 200 μm and (b) 400 μm diameter detector. The Au Lα and Lβ peaks were excluded from this graph due to difficulty deconvolving them. The predicted *FWHM* (dashed line) as computed from the quadratic sum of the calculated electronic noise and the Fano noise, can also be seen.

V. LINEARITY WITH X-RAY INTENSITY

For the energy calibration of the system, the X-ray flux incident on the detector was maximised by setting the Mo target X-ray tube current, X_C, to 1.0 mA. Here, the current of the X-ray tube was varied, to investigate the linearity of the system (count rate) as a function of X-ray fluence.

Additional spectra of two of the fluorescence calibration foils, Zn (Kα = 8.63 keV [51]) and Nb (Kα = 16.61 keV [51]), were accumulated following the same procedure as for the energy calibration of the system, with both $In_{0.5}Ga_{0.5}P$ p^+-i-n^+ mesa photodiodes, to investigate the linearity of the spectrometers as a function of X-ray fluence. The difference between the spectra obtained here, and the spectra obtained for the energy calibration (**Section IV. ENERGY LINEARITY MEASUREMENTS**) was that the Mo target X-ray tube current, X_C, was varied from 0.2 mA to 1.0 mA, in 0.2 mA steps. The detected count rate, R, (in units of counts s^{-1}) defined as the number of counts within the Gaussians fitted to each of the Kα photopeak of Zn (8.63 keV) and Nb (16.61 keV) over the spectrum accumulation time, was determined as a function of X-ray tube current using both photodiodes, and can be seen in **Fig. 7.**

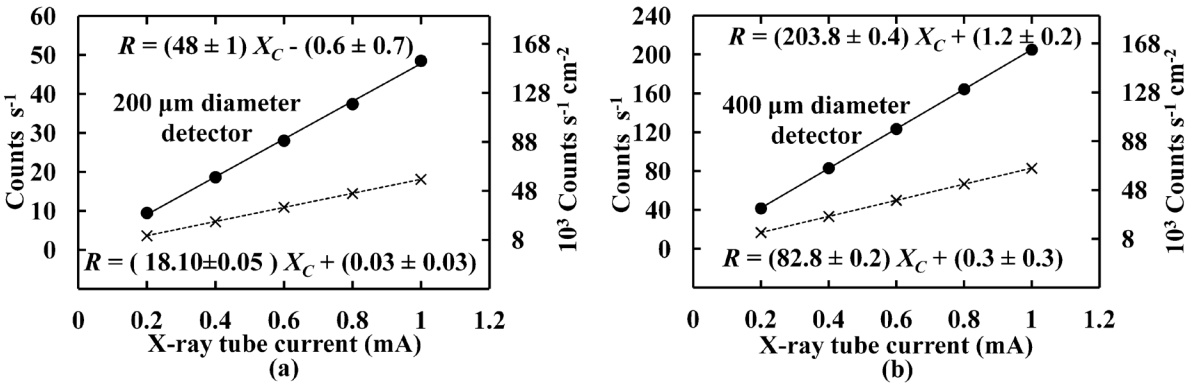

FIG. 7. Count rate within the Gaussian fitted to the Zn Kα (8.63 keV) (circles) and Nb Kα (16.61 keV) (stars) X-ray fluorescence peaks as a function of X-ray tube current using the spectrometer employing the $In_{0.5}Ga_{0.5}P$ (a) 200 µm and (b) 400 µm diameter detector. The lines of best fit, as calculated using linear least squares fitting, can also be seen.

The incident photon fluences can be estimated from the detected count rates and the quantum efficiencies of the detectors. The quantum detection efficiency,

$$QE = [\prod_m \exp(-\mu_m x_m)][1 - \exp(-\mu_{InGaP} x_{InGaP})], \quad (4)$$

of the 200 µm (400 µm) diameter detector was calculated to be 0.2298 (0.2317) at 8.63 keV, and 0.0776 (0.0780) at 16.61 keV. In **Eq. 4**, μ_m and x_m were the linear attenuation coefficient and the thickness of the m^{th} dead layer (Au/Ti contact, and GaAs buffer layer), respectively, and μ_{InGaP} and x_{InGaP} were the linear attenuation coefficient and the thickness of the active layer (p^+ layer and i layer) [52]. The different percentages of the 200 µm and the 400 µm diameter detectors' top faces being covered by the top contacts were considered in the quantum detection efficiency calculations; 33 % and 45 % were covered by the top contacts in the 400 µm diameter and the 200 µm diameter detector, respectively.

Linear relationships were found between the count rates within the Kα photopeak of Zn and Nb and the X-ray tube current. **Figure 7** shows the lines of best fit, calculated using linear least squares fitting. The responses of the spectrometers were found to be linear across the ranges measured. The minimum and maximum investigated incident fluences at 8.63 keV and 16.61 keV, as estimated from the detected count rates and the quantum efficiencies of the detectors for both spectrometers, can be seen in **TABLE III**.

TABLE III. Minimum and maximum detected count rates (given in units of counts s^{-1}) and estimated incident photon fluences (given in units of photons s^{-1} cm^{-2}) at 8.63 keV and 16.61 keV for both spectrometers.

		200 μm diameter detector		400 μm diameter detector	
		Detected counts s^{-1}	Incident photons s^{-1} cm^{-2}	Detected counts s^{-1}	Incident photons s^{-1} cm^{-2}
8.63 keV	min	9	1.3×10^5	42	1.4×10^5
	max	49	6.7×10^5	205	7.0×10^5
16.61 keV	min	4	1.5×10^5	17	1.7×10^5
	max	18	7.4×10^5	83	8.5×10^5

Taking into account the different sizes and *QE* of the detectors, the count rate of the 400 μm detector was expected to be greater than that of the 200 μm detector by a factor of 4.03 at 8.63 keV and 4.02 at 16.61 keV. The experimentally measured count rates however, obtained from the data presented in **Fig. 7**, corresponded to 4.23 at 8.63 keV and 4.58 at 16.61 keV. The differences between the expected and measured values were attributed to slight differences in the placement of each detector within the preamplifier housing rather than differences in their fundamental characteristics.

VI. CONCLUSIONS

Two $In_{0.5}Ga_{0.5}P$ p^+-i-n^+ mesa photodiodes (a 200 μm and a 400 μm diameter device) each with a 5 μm thick i layer, have been investigated for their suitability as detectors for photon counting X-ray spectroscopy within the energy range 4.49 keV and 21.17 keV. The detectors and associated preamplifier electronics were operated uncooled at 30 °C ± 3 °C. The detectors were initially electrically characterized in the temperature range of interest. The diodes were then coupled, each in turn, to the same charge sensitive preamplifier, shaping amplifier,

and MCA. X-ray fluorescence spectra of high-purity calibration samples were accumulated. The samples were fluoresced by a Mo target X-ray tube.

The leakage currents of the packaged $In_{0.5}Ga_{0.5}P$ p^+-i-n^+ mesa photodiodes were ≤ 0.2 pA (≤ 8 e^- rms ENC_{WP} at 6 μs) at the operating reverse bias of -5 V. Packaged devices' capacitances of 1.59 pF ± 0.02 pF (5 e^- rms ENC_{WS} at 6 μs) and 3.58 pF ± 0.02 pF (12 e^- rms ENC_{WS} at 6 μs) were measured for the 200 μm diameter and the 400 μm diameter device, respectively, at -5 V applied bias. Both photodiodes were found to be fully depleted at this applied reverse bias.

For each detector coupled to the spectrometer electronics in turn, linear relationships between the spectrometer charge output and incident photon energy were found across the energy range 4.49 keV and 21.17 keV. The energy resolution (*FWHM*) achievable was found to degrade with increasing photon energy in a manner consistent with Fano noise. Increases in *FWHM* from 0.79 keV ± 0.02 keV at 4.95 keV to 0.83 keV ± 0.02 keV at 21.17 keV, and 1.12 keV ± 0.02 keV at 4.95 keV to 1.15 keV ± 0.02 keV at 21.17 keV were measured using the 200 μm and 400 μm diameter detectors, respectively. The Fano factor of $In_{0.5}Ga_{0.5}P$ was experimentally determined to be 0.13, assuming an electron hole pair creation energy of 4.95 eV at 300 K [27], suggesting a Fano limited energy resolution of 145 eV at 5.9 keV. The number of detected counts per second by both spectrometers was also found to linearly depend on the incident X-ray fluence across the investigated fluence ranges.

All the above results suggested that the $In_{0.5}Ga_{0.5}P$ devices reported here were able to be used for photon counting X-ray spectroscopy at a temperature of 30 °C ± 3 °C, operating uncooled with good energy resolutions and linear responses. This is in contrast to its parent binary compounds, GaP and InP, which have been reported to not be spectroscopic at room temperature [20] [27] [28]. Although the *FWHM* at 5.9 keV achieved with the $In_{0.5}Ga_{0.5}P$ devices were not as good as the best achieved with 4H-SiC (196 eV at 5.9 keV, at 30 °C [6]) and GaAs (266 eV at 5.9 keV, at 23 °C [3]), the $In_{0.5}Ga_{0.5}P$ devices were limited by the noise of the preamplifier electronics rather than the characteristics of the detectors themselves. Improvements in energy resolution would be expected if the $In_{0.5}Ga_{0.5}P$ detectors presented here were coupled to a lower noise preamplifier. However, the energy resolutions (*FWHM* at 5.9 keV) reported here, are already better than those reported using $Cd_{1-x}Zn_xTe$ (e.g. 1.6 keV at 23 °C [24]). $In_{0.5}Ga_{0.5}P$ based spectrometers may find uses in future planetary science and astrophysics space missions, as an alternative to $Cd_{1-x}Zn_xTe$, for the detection of hard X-rays and γ-rays, or for the detection of X-rays and γ-rays in environments of high temperature.

ACKNOWLEDGEMENTS

This work was in part supported by the Science and Technology Facilities Council, United Kingdom, through grants ST/R001804/1 and ST/P001815/1 (A.M.B., PI). A.M.B. acknowledges funding from the Leverhulme Trust, United Kingdom, in the form of a 2016 Philip Leverhulme Prize.

REFERENCES

[1] C.P. Kuo, S.K. Vong, R.M. Cohen, and G.B. Stringfellow, J. Appl. Phys. 57, 5428 (1985).

[2] P.G. Neudeck, R.S. Okojie, and L.-Y. Chen, 2002, Proc. IEEE. 90, 1065 (2002).

[3] A. Owens, M. Bavdaz, A. Peacock, A. Poelaert, H. Andersson, S. Nenonen, H. Sipila, L. Tröger, and G. Bertuccio, J. Appl. Phys. 90, 5376 (2001).

[4] A.M. Barnett, J.E. Lees, D.J. Bassford, J.S. Ng, C.H. Tan, N. Babazadeh, and R.B. Gomes, 2011, Nucl. Instr. Meth. Phys. Res. A 654, 336 (2011).

[5] G. Lioliou, X. Meng, J.S. Ng, and A.M. Barnett, J. Appl. Phys. 119, 124507 (2016).

[6] G. Bertuccio, S. Caccia, D. Puglisi, and D. Macera, Nucl. Instr. Meth. Phys. Res. A 652, 193 (2011).

[7] G. Lioliou, H.K. Chan, T. Gohil, K.V. Vassilevski, N.G. Wright, A.B. Horsfall, and A.M. Barnett, Nucl. Instr. Meth. Phys. Res. A 840, 145 (2016).

[8] S. Zhao, G. Lioliou, and A.M. Barnett, Nucl. Instr. Meth. Phys. Res. A 859, 76 (2017).

[9] A.M. Barnett, J.E. Lees, D.J. Bassford, and J.S. Ng, Nucl. Instr. Meth. Phys. Res. A 673, 10 (2012).

[10] M.D.C. Whitaker, S. Butera, G. Lioliou, and A.M. Barnett, J. Appl. Phys. 122, 034501 (2017).

[11] S. Butera, T. Gohil, G. Lioliou, A.B. Krysa, and A.M. Barnett, J. Appl. Phys. 120, 024502 (2016).

[12] A. Auckloo, J.S. Cheong, X. Meng, C.H. Tan, J.S. Ng, A. Krysa, R.C. Tozer, and J.P.R. David, J. Instrum. 11, P03021 (2016).

[13] A. Owens, H. Andersson, M. Bavdaz, L. van den Berg, A. Peacock, and A. Puig, Nucl. Instr. Meth. Phys. Res. A 487, 90 (2002).

[14] V. Kozlov, H. Andersson, V. Gostilo, M. Leskelä, A. Owens, M. Shorohov, and H. Sipilä, Nucl. Instr. Meth. Phys. Res. A 591, 209 (2008).

[15] S.U. Egarievwe, K.T. Chen, A. Burger, R.B. James, and C.M. Lisse, J. Xray Sci. Technol. 6, 309 (1996).

[16] C.T.C. Hansson, A. Owens, and J. van den Biezen, Acta Astronaut. 93, 121 (2014).

[17] A. Zappettini, D. Macera, G. Benassi, N. Zambelli, D. Calestani, M. Ahangarianabhari, Y. Shi, G. Rotondo, B. Garavelli, P. Pozzi, and G. Bertuccio, IEEE Nucl. Sci. Symp. Conf. NSS/MIC 2014 (2016).

[18] M. Kondow, H. Kakibayashi, S. Minagawa, Y. Inoue, T. Nishino, and Y. Hamakawa, Appl. Phys. Lett. 53, 2053 (1988).

[19] A. Owens, A.J. Peacock, and M. Bavdaz, SPIE proceedings of X-ray and Gamma-Ray Telescopes and Instruments for Astronomy 4851, 1059 (2003).

[20] F. Dubecký, B. Zat'ko, V. Nečas, M. Sekáčová, R. Fornari, E. Gombia, P. Boháček, M. Krempaský, and P. G. Pelfer, Nucl. Instr. Meth. Phys. Res. A 487, 27 (2002).

[21] J.H. Hubbell, and S.M. Seltzer, *Tables of X-Ray Mass Attenuation Coefficients and Mass Energy-Absorption Coefficients (version 1.4)* (National Institute of Standards and Technology, Gaithersburg, MD, 2004).

[22] S.D. Barthelmy, L.M. Barbier, J.R. Cummings, E.E. Fenimore, N. Gehrels, D. Hullinger, H.A. Krimm, C.B. Markwardt, D.M., Palmer, A., Parsons, G., Sato, M., Suzuki, T., Takahashi, M., Tashiro, and J., Tueller, Space Sci. Rev. 120, 143 (2005).

[23] M. Kokubun, S. Watanabe, K. Nakazawa, H. Tajima, Y. Fukazawa, T. Takahashi, J. Kataoka, T. Kamae, H. Katagiri, G.M. Madejski, K. Makishima, T. Mizuno, M. Ohno, R. Sato, H. Takahashi, T. Tanaka, M. Tashiro, Y. Terada, and K. Yamaoka, Nucl. Instr. Meth. Phys. Res. A 623, 425 (2010).

[24] A. Owens, M. Bavdaz, H. Andersson, T. Gagliardi, M. Krumrey, S. Nenonen, A. Peacock, I. Taylor, and L. Tröger, Nucl. Instr. Meth. Phys. Res. A 484, 242 (2002).

[25]M. Sammartini, M. Gandola, F. Mele, B. Garavelli, D. Macera, P. Pozzi, and G. Bertuccio, Nucl. Instr. Meth. Phys. Res. A 910, 168 (2018).

[26] S. Butera, G. Lioliou, A.B. Krysa, and A.M. Barnett, Sci. Rep. 7, 10206 (2017).

[27] S. Butera, G. Lioliou, A.B. Krysa, and A.M. Barnett, Nucl. Instr. Meth. Phys. Res. A 908, 277 (2018).

[28] A. Owens, S. Andersson, R. den Hartog, F. Quarati, A. Webb, and E. Welter, Nucl. Instr. Meth. Phys. Res. A 581, 709 (2007).

[29] A. Owens, M. Bavdaz, V. Gostilo, D. Gryaznov, A. Loupilov, A. Peacock, and H. Sipila, Nucl. Instr. Meth. Phys. Res. A 487, 435 (2002).

[30] Y. Fukuda, T. Izawa, Y. Koshio, S. Moriyama, T. Namba, and M. Shiozawa, Nucl. Instr. Meth. Phys. Res. A 623, 460 (2010).

[31] P.G. Pelfer, F. Dubecky, R. Fornari, M. Pikna, E. Gombia, B. Zatko, J. Darmo, M. Krempasky, and M. Sekacova, proceedings of the 3rd International EuroConference on Advanced Semiconductor Devices and Microsystems, 99 (2000).

[32] R.S. Raghavan, Phys. Rev. Lett. 37, 259 (1976).

[33] T. Suzuki, A. Gomyo, and S. Iijima, J. Cryst. Growth 93, 396 (1988).

[34] S. Minagawa, and M. Kondow, Electron. Lett. 25, 758 (1989).

[35] Keysight Technologies, Inc., *B2980A Series Femto/Picoammeter and Electrometer/High Resistance Meter*, 5991-4878 (California, 2016).

[36] Keithley Instruments, Inc., *Models 2634B, 2635B and 2636B System SourceMeter Instrument Specifications*, SPEC-2636B Rev. B (Ohio, 2013).

[37] Hewlett Packard, *Model HP 4275A Multi-Frequency LCR Meter Operating Manual*, 04275-90004 (Tokyo, 1979).

[38] Keithley Instruments, Inc., *Model 6487 Picoammeter/Voltage Source Reference Manual*, 6487-901-01 Rev C (Ohio, 2011).

[39] S.M. Sze, and K.K. Ng, *Physics of Semiconductor Devices* (John Wiley & Sons, New Jersey, 2007) 3rd ed..

[40] G. Bertuccio, P. Rehak, and D. Xi, Nucl. Instr. Meth. Phys. Res. A 326, 71 (1993).

[41] Siliconix, *2N4416/2N4416A/SST4416 N-Channel JFETs*, Data Sheet, 70242 S-04028, Rev. F, 04-Jun-01 (Vishay Electronic GmbH, Selb, 2001).

[42] LD Didactic, GmbH., *X-ray apparatus (554 800)*, Instruction sheet 554 800 (Huerth, 2014).

[43] N.R. Draper, and H. Smith, *Applied Regression Analysis* (John Wiley & Sons, New York, 2014) 3rd ed..

[44] M. Sánchez del Rio, A. Brunetti, B. Golosio, A. Somogyi, and A. Simionovici, *XRAYLIB Tables (X-ray Fluorescence Cross-Section)* (European Synchrotron Radiation Facility and University of Sassari, 2003).

[45] G. Lioliou, and A.M Barnett, Nucl. Instr. Meth. Phys. Res. A 801, 63 (2015).

[46] U. Fano, Phys. Rev. 72, 26 (1947).

[47] B.G. Lowe, Nucl. Instr. Meth. Phys. Res. A 399, 354 (1997).

[48] G. Bertuccio, A. Pullia, J. Lauter, A. Forster, and H. Luth, IEEE Trans. Nucl. Sci. 44, 1 (1997).

[49] A. Owens, M. Bavdaz, A. Peacock, A. Poelaert, H. Andersson, S. Nenonen, L. Tröger, and G. Bertuccio, Nucl. Instr. Meth. Phys. Res. A 466, 168 (2001).

[50] T. Takahashi, S. Watanabe, M. Kouda, G. Sato, Y. Okada, S. Kubo, Y. Kuroda, M. Onishi, and R. Ohno, IEEE Trans. Nucl. Sci. 48, 287 (2001).

[51] A. Thompson, D. Attwood, E. Gullikson, M. Howells, K.J. Kim, J. Kirz, J. Kortright, I. Lindau, Y. Liu, P. Pianetta, A. Robinson, J. Scofield, J. Underwood, G. Williams, and H. Winick, *X-Ray Data Booklet (Center for X-Ray Optics and Advanced Light Source)* (Lawrence Berkeley National Laboratory, Berkeley, 2009).

[52] G.W. Fraser, *X-ray Detectors in Astronomy* (Cambridge University Press, Cambridge, 1989).